In vitro quantification of metal ion specificity of *Cc*NikZ-II in the presence of competing metal ions

Patrick Diep[1,*], Brayden Kell[2,3,*], Alexander Yakunin[1,4], Andreas Hilfinger[2,3,5,6], and Radhakrishnan Mahadevan[1,7]

[1]BioZone Centre for Applied Bioscience and Bioengineering, Department of Chemical Engineering and Applied Chemistry, University of Toronto, Toronto, Canada
[2]Department of Physics, University of Toronto, Toronto, Canada
[3]Department of Chemical and Physical Sciences, University of Toronto Mississauga, Mississauga, Canada
[4]Centre for Environmental Biotechnology, Bangor University, Bangor, United Kingdom
[5]Department of Mathematics, University of Toronto, Toronto, Canada
[6]Department of Cell and Systems Biology, University of Toronto, Toronto, Canada
[7]Institute for Biomedical Engineering, University of Toronto, Toronto, Canada
[*]These authors contributed equally to this work and retain the right to exchange the order of their names in citing this work.

ABSTRACT

Many proteins bind transition metal ions as cofactors to carry out their biological functions. Despite wild-type binding affinities for transition metal ions being predominantly dictated by the Irving-Williams series, *in vivo metal* ion binding specificity is ensured by intracellular mechanisms that regulate free metal ion concentrations. However, a growing area of biotechnology research considers the use of metal-binding proteins *in vitro* to purify specific metal ions from wastewater, where specificity is dictated by the protein's metal binding affinities. A goal of metalloprotein engineering is to modulate these affinities to improve a protein's specificity towards a particular metal; however, the quantitative relationship between the affinities and the equilibrium metal-bound protein fractions depends on the underlying binding kinetics. Here we demonstrate a high-throughput intrinsic tryptophan fluorescence quenching method to validate kinetic models in multi-metal solutions for *Cc*NikZ-II, a metal-binding protein from *Clostridium carboxidivorans*. Using our validated models, we quantify the relationship between binding affinity and specificity in different classes of metal-binding models for *Cc*NikZ-II. We further demonstrate that principles for improving specificity through changes in binding specificity are qualitatively different depending on the competing metals, highlighting the power of mechanistic models to guide metalloprotein engineering targets.

***K*eywords** metalloproteins · binding kinetics · model validation · protein design

1 Introduction

Many proteins rely on a metal ion (herein 'metal') cofactors to carry out their biological function [1]. Organic molecules like proteins have a strong tendency towards forming the highest affinity complexes with Cu^{II}, whereas the lowest affinity is observed for complexes with Mn^{II} and Fe^{II}. More generally, metal-binding affinities of wild-type proteins are predominantly dictated by the Irving-William series: $Mg^{II} < Mn^{II} < Fe^{II} < Co^{II} < Ni^{II} < Cu^{II} > Zn^{II}$ [2, 3]. To ensure correct metalation of proteins *in vivo* for biological function despite this hierarchy, cells have specifically evolved intracellular metal-sensing systems that control their internal metal concentrations [4, 5].

The selectivity of a protein's metal binding site is determined by the electronic properties of amino acid residues that are spatially coordinated to accommodate a metal's preferred coordination geometry [6, 7]. These residues comprise the primary coordination sphere, and further contributions from the secondary coordination sphere and overall protein matrix can exert additional metal specificity [6, 8]. The dissociation constant, K_D, is a thermodynamic parameter used to quantify the binding affinity for a particular metal-protein pair. These quantities are often reported as *apparent* dissociation constants under specific pH and buffering conditions [9]. Determination of dissociation constants is often

accomplished by purifying the protein [10, 11], then titrating it to saturation with the metal while following the response of a fluorescence probe. The probe can either be the protein itself through intrinsic fluorescence quenching [12, 13] or an added molecular probe with fluorescence properties [9, 14].

For metals that bind the protein with high affinity, it can be difficult to reliably estimate the K_{D} value with direct metal titration experiments [14]. In such cases, competition experiments are used to determine the K_{D} instead. Competition may be achieved either by adding a molecule that competes with the protein for the metal or a second metal that competes with the metal for the protein [5, 15–21]. In the latter case, an unbound protein P is first saturated with metal X, then titrated with another metal Y. Under such conditions, the binding competition is described by the displacement reaction $PX + Y \rightleftharpoons PY + X$. Some have used this technique to study the two metals' relative affinity described by the equilibrium constant for the exchange reaction $K_{\mathrm{ex}} = K_{\mathrm{D(X)}}/K_{\mathrm{D(Y)}}$ (herein 'exchange constant'). The exchange constant is used in some studies to quantify the competition between two metals for binding a given protein [17–19].

However, the quantitative relationship between K_{ex} and *in vitro* protein metalation fractions in a multi-metal solution remains unclear in general. While, methodologies have been developed to calculate fractions of a protein bound to these different metals *in vivo* [4, 5], a growing area of biotechnology research considers the use of metalloproteins *in vitro* to purify specific metals from wastewater containing several metals in large excess [22–24]. A quantitative grasp of this relationship could thus enable model-guided design of metalloproteins towards more selective biotechnologies in bio-based metal purification.

Towards this end, we present an experimental approach relying on intrinsic tryptophan fluorescence quenching (ITFQ) to evaluate the ability of candidate models to predict a protein's binding curves in multi-metal solutions. We used this approach to validate models of binding competition for purified *Cc*NikZ-II in two-metal solutions. In solutions of Ni^{II}+Co^{II}, we found a model where both metals bind a single binding site on on *Cc*NikZ-II predicted the measured binding curves adequately. However, this model did not adequately predict *Cc*NikZ-II's binding curves in solutions of Ni^{II}+Zn^{II}. In this case, we found a model including two binding sites better described the data. With the validated models, we derived predictions for the competitor-bound protein fraction at equilibrium for each two-metal solution. We demonstrated that the exchange constant does not uniquely determine the competitor-bound protein fraction at equilibrium in our model and predict that hypothetical changes in the K_{D} values for each metal has distinct quantitative effects on this quantity, depending on the underlying binding dynamics. Together, this work delineates a new approach for quantitatively understanding metalloprotein binding specificity in multi-metal solutions.

2 Methods

2.1 Binding model for single-metal solutions

We modelled the single-metal systems as well-mixed aqueous buffer solutions containing a metalloprotein P and a metal species M. If M binds a single binding site on P with one-to-one stoichiometry (Sect. 3.1), such a system is described by the simple equilibrium reaction

$$MP \rightleftharpoons M + P \tag{1}$$

with equilibrium (dissociation) constant

$$K_{\mathrm{D}(M)} \coloneqq \frac{[M][P]}{[MP]}\ , \tag{2}$$

where $[\cdot]$ denotes an equilibrium concentration. The three equilibrium concentrations for such a system are specified by the empirical $K_{\mathrm{D}(M)}$ value and the mass balance equations

$$\begin{aligned} [M]_{\text{total}} &\coloneqq [M] + [MP] \\ [P]_{\text{total}} &\coloneqq [P] + [MP]\ . \end{aligned} \tag{3}$$

The following relationship between the measured tryptophan fluorescence quenching signal to $K_{\mathrm{D}(M)}$ and the (known) $[M]_{\text{total}}$ and $[P]_{\text{total}}$ was previously derived for this system:

$$\frac{\overbrace{F_0 - F}^{=:F_{\text{obs}}}}{\underbrace{F_0 - F_c}_{=:F_{\text{max}}}} = \frac{[MP]}{[P]_{\text{total}}} \tag{4}$$

$$= \frac{[M]_{\text{total}} + [P]_{\text{total}} + K_{\mathrm{D}(M)} - \sqrt{\left([M]_{\text{total}} + [P]_{\text{total}} + K_{\mathrm{D}(M)}\right)^2 - 4[M]_{\text{total}}[P]_{\text{total}}}}{2[P]_{\text{total}}}\ , \tag{5}$$

where F_0 and F_c are the fluorescence intensities measured when all protein molecules are unbound and bound, respectively, and F is the fluorescence intensity measured at occupancy fractions between 0% and 100% [25–27]. Thus, at fixed $[P]_{\text{total}}$ values, experimental measurements of F_{obs} for varying $[M]_{\text{total}}$ values can be used to estimate the parameters $K_{\text{D}(M)}$ and F_{max} via curve fitting.

2.2 Single-site binding model for multi-metal solutions

We modelled the multi-metal systems involving a single protein binding site as well-mixed aqueous buffer solutions containing a metalloprotein P and $N > 1$ metal species M_i $(i = 1, \ldots, N)$ that all bind the same site on the protein. While we restrict our experiments to two-metal systems in this work, we present our multi-metal models for arbitrarily many competing metals for generality. If each metal binds with one-to-one stoichiometry, such a system is described by the set of coupled equilibrium reactions

$$M_iP \rightleftharpoons M_i + P \,, \qquad i = 1, \ldots, N \tag{6}$$

with equilibrium (dissociation) constants

$$K_{\text{D}(M_i)} \coloneqq \frac{[M_i][P]}{[M_iP]} \,, \qquad i = 1, \ldots, N \,. \tag{7}$$

If each metal results in the same degree of fluorescence quenching upon binding, we found Eq. (4) generalized to the following (Supplementary Information Sect. S1.1):

$$\frac{F_{\text{obs}}}{F_{\text{max}}} = \frac{\sum_{i=1}^{N}[M_iP]}{[P]_{\text{total}}} \,. \tag{8}$$

There is no general parametric solution analogous to Eq. (5) for arbitrary N values (Supplementary Information Sect. S1.1). However, such parametric solutions can be obtained for particular $N \leq 3$. For larger N, numerical techniques have been developed to obtain numerical solutions given given specified values of $[P]_{\text{total}}$, $K_{\text{D}(i)}$ and $[M_i]_{\text{total}}$ for each i [28, 29]. Thus, if $K_{\text{D}(i)}$ are known from independent single-metal fluorescence quenching experiments, then Eq. (8) permits an exact theoretical prediction that may be compared against experimental data of the fluorescence signal for varied total metal concentrations at fixed total protein levels to validate the mathematical model.

2.3 Two-site binding model for multi-metal solutions

As in Sect. 2.2, we modelled the multi-metal systems involving a second protein binding site as well-mixed aqueous buffer solutions containing a metalloprotein P and $N > 1$ metal species M_i $(i = 1, \ldots, N)$. However, here we considered the case where each metal M_i to bind exactly one of the two binding sites on the protein, as indicated by the sets

$$S_1 \coloneqq \{i \mid M_i \text{ binds site 1}\} \tag{9}$$

$$S_2 \coloneqq \{i \mid M_i \text{ binds site 2}\} \,. \tag{10}$$

If each metal binds with one-to-one stoichiometry, such a system is described by the set of coupled equilibrium reactions

$$M_iP \rightleftharpoons M_i + P \,, \qquad i = 1, \ldots, N \tag{11}$$

with equilibrium (dissociation) constants

$$K_{\text{D}(M_i)} \coloneqq \frac{[M_i][P]}{[M_iP]} \,, \qquad i = 1, \ldots, N \,. \tag{12}$$

However, the presence of the second site permits the formation of higher-order complexes via

$$M_iM_jP \rightleftharpoons M_i + M_j + P \,, \qquad i \in S_1,\ j \in S_2 \,. \tag{13}$$

In the absence of allosteric interactions, the equilibrium constants for these reactions are constrained by

$$\frac{[M_i][M_j][P]}{[M_iM_jP]} = K_{\text{D}(i)}K_{\text{D}(j)} \,, \qquad (i,j) \in S_1 \times S_2 \,, \tag{14}$$

where $\times$ denotes the Cartesian product. If each metal in S_1 results in the same degree of fluorescence quenching upon binding, and likewise for each metal in S_2 (though, not necessarily as for those in S_1), we found Eq. (4) generalized to the following (Supplementary Information Sect. S1.2):

$$F_{\text{obs}} = \frac{F_{\text{max}}^{(1)}\sum_{i\in S_1}[M_iP] + F_{\text{max}}^{(2)}\sum_{i\in S_2}[M_iP] + F_{\text{max}}^{(1,2)}\sum_{(i,j)\in S_1\times S_2}[M_iM_jP]}{[P]_{\text{total}}} \,, \tag{15}$$

where $F_{\text{max}}^{(j)}$ ($j = 1, 2$) corresponds to the fluorescence signal if site j is fully saturated and $F_{\text{max}}^{(1,2)}$ corresponds to the fluorescence signal if both site 1 and site 2 are fully saturated. Like in the single-site model, parametric solutions can only be obtained for $N < 3$, but the numerical solution algorithm in [29] may be used to obtain numerical solutions for specified values of $[P]_{\text{total}}$, $K_{\text{D}(i)}$ and $[M_i]_{\text{total}}$ for each i. Since this equation depends on an additional parameter $F_{\text{max}}^{(1,2)}$ related to the formation of the second-order complexes M_iM_jP for $i \neq j$, predictions based on parameters inferred from single-metal experiments alone are not permissible. Thus, we treated $F_{\text{max}}^{(1,2)}$ as a fit parameter in our analysis.

2.4 Parameter estimation and data analysis

Averages and standard deviations across three technical replicates of each experiment were calculated from the raw fluorescence data (Sect. 2.8) in `Microsoft Excel`. K_{D} and F_{max} values were then estimated from these data for single-metal experiments by least-squares optimization of Eq. (5) using the `scipy` library in in `Python 3.8.5` (Table 1). Theoretical predictions of equilibrium concentrations for the multi-metal experiments were obtained in Wolfram Mathematica 12 by first solving for theoretical equilibrium concentrations from the mass balance and K_D equations for the appropriate multi-metal model (either the single-site or the two-site multi-metal binding model, depending on the metal solution composition) and substituting the K_{D} values inferred from the single-metal data for each metal species (Supplementary Information Sect. S1.4). For model validation in the Ni^{II}+Co^{II} systems, theoretical equilibrium concentrations were calculated for the single-site multi-metal model (Sect. 2.2) across the range of total metal and protein concentrations used in the titration and substituted into Eq. (8) with the total protein concentration and the F_{max} value estimated from the single-metal experiments, resulting in a predicted F_{obs} signal for the given experimental parameters. For model validation in the Ni^{II}+Zn^{II} systems, theoretical equilibrium concentrations were calculated for the two-site multi-metal model (Sect. 2.3) across the range of total metal concentrations used in the titration and substituted into Eq. (15) with the total protein concentrations. Additionally, $F_{\text{max}}^{(1)}$ and $F_{\text{max}}^{(2)}$ were set to the F_{max} value estimated from the single-metal experiments for Ni and Zn, respectively. Since $F_{\text{max}}^{(1,2)}$ cannot be inferred from single-metal experiments, this parameter was estimated by least-squares optimization of Eq. (15) using the `scipy` in `Python 3.8.5` (Table 2). Reduced χ^2 (χ_r^2) values were calculated to assess the agreement of both fitted and predicted curves with the data [30] (Table 1, Table 2, Supplementary Tables S1-S4).

2.5 DNA synthesis, cloning, and strains

The open-reading frame encoding *Cc*NikZ-II from *C. carboxidivorans* P7T (Ccar_RS11695, NCBI ID: NZ_CP011803.1) was synthesized (Twist Bioscience, San Francisco, USA) without its native signal peptide identified using SignalP 5.0 with the Gram-positive setting [31]. This was cloned into p15TV-L (AddGene ID: 26093) under the T7 promoter in-frame with the N-terminal 6xHisTag, then transformed into a LOBSTR (Kerafast, #EC1001) *Escherichia coli* strain and subsequently plated onto LB-Agar (carbenicillin, 100 µg/mL). Plasmids were sequencenegativerified at the ACGT Sequencing Facility (Toronto, Canada). Glycerol stocks were stored at -80 °C.

2.6 Protein expression and purification

This protocol is based on prior work [32]. Starter cultures of *Cc*NikZ-II were grown from glycerol stock in LB with carbenicillin (100 µg/mL) for 16 h overnight at 37 °C with shaking. Expression cultures were started by pre-warming TB media with 5% glycerol and carbenicillin (100 µg/mL) to 37 °C before 1% v/v inoculation with the starter culture, then grown for 5 hr at 37 °C until addition of IPTG (BioShop, #IPT002) to 0.4 mM for induction. The expression cultures were then transferred to 16 °C and grown for 16 hr overnight with shaking, then pelleted with centrifugation and transferred to conical vials for one freeze-thaw cycle at -20 °C.

Frozen cell pellets were thawed and resuspended in binding buffer (10 mM HEPES, 500 mM NaCl, 5 mM imidazole, pH 7.2) to a final volume of 100 mL, followed by addition of 0.25 g lysozyme (BioShop, #LYS702). Cell pellet mixtures were sonicated for 15 min (Q700 Sonicator, Qsonica) and clarified by centrifugation. The soluble layer (supernatant) was applied to a cobalt-charged (Co-)NTA resin (Thermo Fisher, #88221) pre-equilibrated with binding buffer in a gravity-column set-up. Bound proteins were cleansed with wash buffer (10 mM HEPES, 500 mM NaCl, 25 mM imidazole, pH 7.2) and the bound protein was collected with elution buffer (10 mM HEPES, 500 mM NaCl, 250 mM imidazole, pH 7.2). Protein concentrations were determined by BCA assay, and protein purity was determined by SDS-PAGE analysis and densitometry on Image Lab 6.0 (Bio-Rad).

Eluted protein was combined with 0.4 mg of in-house purified TEV protease and DTT to 1 mM (BioShop, #TCE101), then transferred to a 10 kDa MWCO dialysis bag (Thermo Fisher, #68100) for dialysis in 4 L dialysis buffer (10 mM HEPES, 1 mM TCEP, 1 g/L Chelex 100, pH 7.2) at 4 °C with gentle stirring for 24 hr. Dialyzed samples were then applied to a cobalt-charged NTA resin twice and transferred to a 10 kDa MWCO dialysis bag for dialysis in 4 L dialysis

buffer (10 mM HEPES, pH 7.2) at 4 °C with gentle stirring for 24 hr and transferred to fresh dialysis buffer for another 24 hr. Finally, samples were flash-frozen in 200 µL aliquots in liquid nitrogen before storage at -80 °C.

2.7 Preparation of activity buffers and metal solutions

Nickel and cobalt solutions were prepared from hexahydrate chloride salts $NiCl_2$ (BioShop, #NIC999.500) and $CoCl_2$ (BioShop, #COB001.100) in non-buffered deionized MilliQ water. The concentrations were then determined by ICP-MS to be 73.24 mM Ni^{II} and 78.34 mM Co^{II}, respectively (see Section 2.10). Nickel, cobalt, and Ni^{II}+Co^{II} working solutions were then made for experiments from these stock solutions using activity buffer ("AB", 10 mM HEPES, pH 7.2) previously prepared from deionized MilliQ water adjusted to the desired pH using NaOH, then filter sterilized by syringe using a 0.2 µm PTFE membrane disc (PALL, #4187). The pH of the working solutions were unchanged based on visual inspection by litmus paper, which was expected based on `OLI Studio 9.6` simulations. Additionally, more than 99% of the metals were in the aqueous phase based on `OLI` calculations for all metal concentrations used (between 0 to 0.7 mM).

2.8 Determination of $K_{\mathbf{D}}$ by intrinsic tryptophan fluorescence quenching

The microplate-based intrinsic tryptophan fluorescence quenching ligand-titration assay (microITFQ-LTA) is based on prior work [32]. Binding assays were performed in black, opaque 96-well microplates (Greiner Bio-One, #655076) using the Infinite® 200 PRO (Tecan) plate reader with the following settings: fluorescence top-read, 25 °C, $\lambda_{ex} = 280$ nm, $\lambda_{em} = 380$ nm, and manual gain of 100.

The general procedure used to obtain binding curves first required 150 µL of 0.4 µM *Cc*NikZ-II in AB to be added to a well and equilibrated for 20 min with shaking (orbital, 3mm) to 25 °C. The baseline fluorescence was monitored to ensure equilibration, from which one endpoint reading was made as the blank (F_0). Step-wise titrations of metal working solution were added until saturation. At each titration step, a small aliquot (1 to 20 µL) is added by multi-channel pipette, then equilibrated for 3 min with shaking (orbital, 3mm). For larger aliquots (10 to 20 µL), the samples were equilibrated for at least 5 min with shaking (orbital, 3mm) or until the fluorescence stabilized. At each titration step, after the equilibration period, the fluorescence was measured (F). The protein and metal concentrations vary depending on the experiment as outlined in the main text. Experiments were performed in triplicates.

Mixing by pipette was avoided to prevent the introduction of air bubbles or the unintentional removal of protein due to droplets sticking to the inside of tips. To account for possible dilution effects, we included a triplicate negative control where the protein was titrated with AB-only using the same volumes added at each titration step. The inner-filter effect was not observed for the metal working solutions.

2.9 Determination of metal-protein stoichiometry by fractionation

A 1:100 protein-metal solution (1 mL) containing 1.7 µM *Cc*NikZ-II (0.1 µg/mL) and 170 µM Ni^{II} in AB was prepared and transferred to the upper portion of a 10 kDa MWCO concentrator (Cytiva, #28932296). This was then placed into a temperature-controlled centrifuge where it was first equilibrated for 30 min at 25 °C without disturbance, then suddenly centrifuged at 2000 rpm for 15 min. The initial permeate (labelled FT for flow-through) was transferred to a pre-weighed microfuge tube. To wash the retentate, 1 mL of AB was added to the retentate and quickly centrifuged again, as described above. The first wash permeate was transferred to another pre-weighed microfuge tube. This wash process was repeated twice for a total of three washes to create three wash permeates (labelled W1, W2, and W3). The masses of FT, W1, W2, and W3 were determined by subtracting the pre-recorded initial tube weights. The volume of each fraction was calculated assuming a density of 1 g/mL. Negative controls were included where either *Cc*NikZ-II, Ni^{II}, or both were absent. The experiment was performed in duplicates. The metal concentration was determined for each fraction by ICP-MS (see Section 2.10), and the protein concentration was determined by BCA assay, following the manufacturer protocol (Thermo Fisher, #23227).

2.10 Metal analysis by ICP-MS

Metal concentrations were determined by inductively coupled plasma mass spectrometry (ICP-MS) using a Thermo Scientific™ iCAP Q ICP-MS system in kinetic energy discrimination (KED) mode. Samples were prepared by dilution into a 2% HNO_3 solution made from deionized MilliQ water and ultrapure HNO_3 Optima™ (Fisher Chemical, #S020101TFIF01). Nickel and cobalt calibration curves were created using ICP-grade nickel (Millipore Sigma, #28944) and cobalt (Millipore Sigma, #30329) standards. 0, 20, 100, 500, and 1000 ppb metal standards were prepared with glass volumetric flasks and pipettes previously triple-washed with 10% HNO_3 TraceMetal™ (Fisher Chemical, #S010101TFIQ03).

3 Results & Discussion

3.1 Single-metal experiments to determine stoichiometry and K_{D} of *Cc*NikZ-II

*Cc*NikZ-II is homologous to the solute-binding component of *Campylobacter jejuni*'s nickel-specific ABC transporter, which is involved in enzymatic processes requiring nickel-based cofactors [33, 34]. Indeed, in prior work we demonstrated *Cc*NikZ-II binds to Ni^{II}, as expected [32]. Additionally, our prior work suggests Ni^{II} binds *Cc*NikZ-II with 1:1 stoichiometry based on a fitted Hill coefficient [32]. Here, we sought to directly measure the ratio of protein-bound Ni^{II} to Ni^{II}-bound protein to verify this inference. *Cc*NikZ-II from *C. carboxidivorans* was recombinantly expressed in *E. coli* cells and affinity purified to over 95% homogeneity (Sect. 2.5, 2.6). To determine the Ni^{II} binding stoichiometry of *Cc*NikZ-II, the purified protein was pre-incubated in excess Ni^{II} (1:100), and the unbound ions were washed out using centrifugal filters. Virtually no Ni^{II} or *Cc*NikZ-II protein was observed in controls where they were not added (Fig. 1AB, Supplementary Table S3). The empirical stoichiometric ratio between Ni^{II} and *Cc*NikZ-II across the two technical replicates was 1.18 and 0.91 (Fig. 1C), which provided experimental evidence to support the modelling assumption of 1:1 metal-binding to *Cc*NikZ-II.

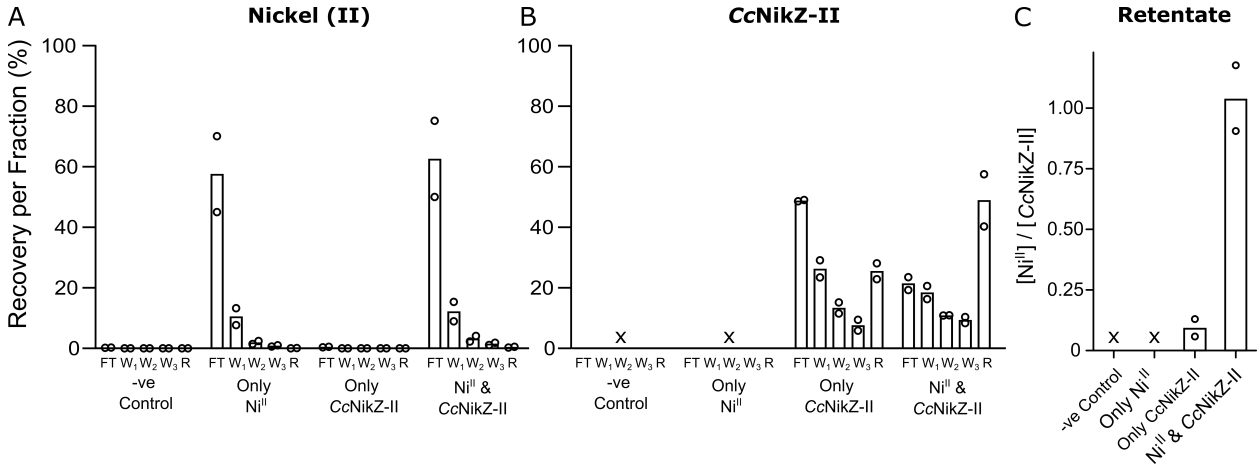

Figure 1: **Stoichiometry determination by fractionation.** FT - Flow through, W1 - Wash 1, W2 - Wash 2, W3 - Wash 3, R - Final Retentate. "x" denotes where calculations could not be made due to the protein concentration being below the limit of detection. (A) Recovery of nickel per fraction determined by ICP-MS, (B) Recovery of protein per fraction determined by BCA assay, (C) Final molar stoichiometry of Ni^{II} to *Cc*NikZ-II in retentate after W3. Experiments were performed in duplicates, n=2. Bars indicate the average across the replicates, open circles correspond to the raw data.

We then determined the K_{D} values of *Cc*NikZ-II for nickel, cobalt, and zinc each using the microITFQ-LTA and fitting the data to Eq. (5) (Fig. 2). Similar to results in Diep *et al.* (2020), we observed *Cc*NikZ-II had higher affinity for nickel than cobalt or zinc (Table 1), which is consistent with the Irving-William series (see Sect. 1). We also note that *Cc*NikZ-II had a similar $F_{\max}$ value for both nickel and cobalt, which suggested the polar environments surrounding *Cc*NikZ-II's tryptophan moieties undergo similar changes upon binding to either metal, consistent with a single-site binding model (see Sect. 3.2). Conversely, *Cc*NikZ-II's $F_{\max}$ value differed significantly between nickel and zinc experiments, which was previously observed in [32].

Table 1: Fitted Parameters and χ^2_r from Single-metal Experiments

		K_{D} (μM)	$F_{\max}$ (a.u.)	χ^2_r
Single-metal experiments (Fig. 2)	Ni^{II}	10.4 ± 1.4	738.8 ± 24.1	0.6
	Co^{II}	37.0 ± 3.7	743.9 ± 23.8	0.3
	Zn^{II}	33.7 ± 3.4	1043.1 ± 27.9	0.4

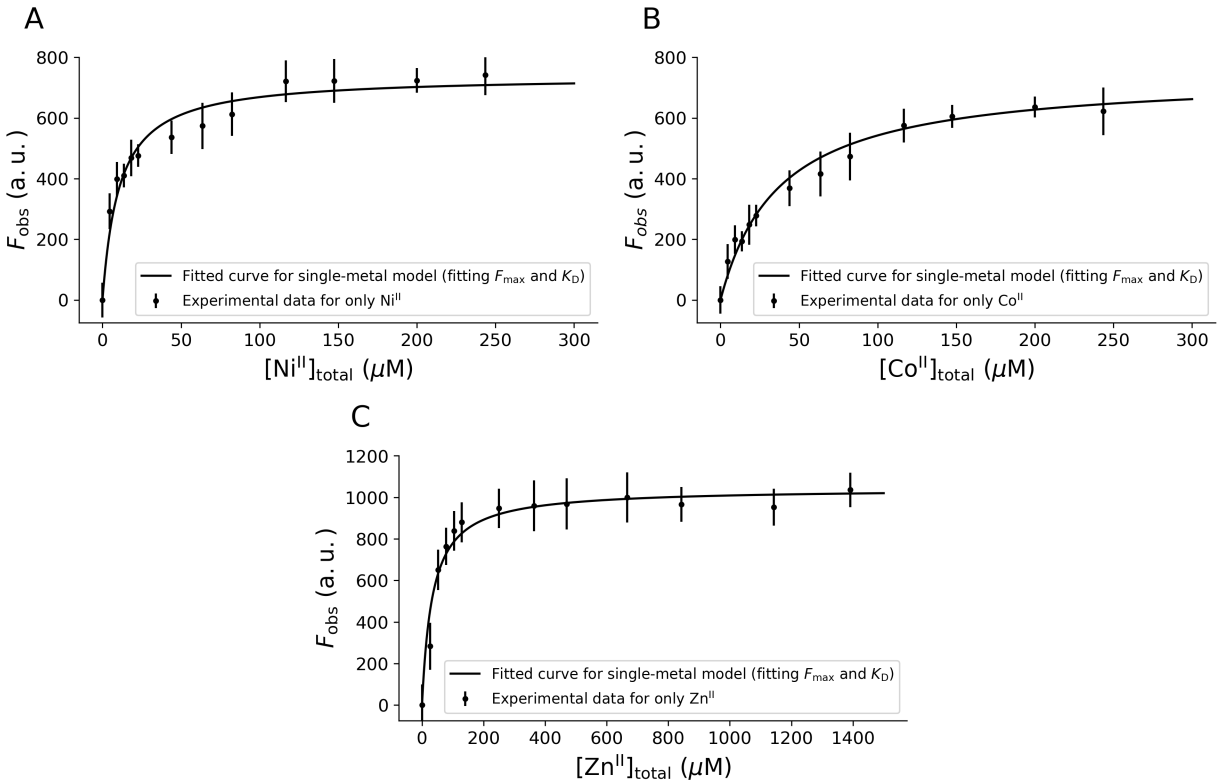

Figure 2: **Independent binding curves of *Cc*NikZ-II separately titrated with nickel (A), cobalt (B), or zinc (C)**. The binding curves shown correspond to Eq. (5) evaluated for the K_D and F_{max} inferred via least squares optimization to the data (Table 1). Experiments were performed in triplicate, n=3. The dots and error bars denote the mean and standard deviation, respectively, across the technical replicates for each titration step.

3.2 Model validation by comparison of predicted binding curves to data in two-metal solutions

After estimating the K_D and F_{max} values for each of nickel, cobalt, and zinc, we sought to assess the ability of our models to predict binding curves for *Cc*NikZ-II in the presence of nickel and cobalt or nickel and zinc at varied total concentrations of the competitor (cobalt or zinc) relative to the total nickel concentration.

First, we assessed the ability of the single-site model (Sect. 2.2) to predict binding curves for *Cc*NikZ-II in solutions with nickel and cobalt (Fig. 3). To obtain such binding curves, we titrated the protein with metal stock solutions containing a mixture of the two metals at total metal ratios $f_{Co} := [Co^{II}]_{total}/[Ni^{II}]_{total} = 0.1$, 0.5, 1.0, 2.0, and 10.0. F_{obs} was measured for each f_{Co} value over $[Ni^{II}]_{total}$ values between 0 μM and 250μM with $[P]_{total} = 0.4$ μM. We then generated binding curve predictions from the single-site model (Sect. 2.2) across the range of titrations for the $K_{D(Ni^{II})}$, $K_{D(Co^{II})}$, and F_{max} values determined in Sect. 3.1 (Table 1). The value of F_{max} used to parameterize the model was the average of the inferred values for Ni^{II} and Co^{II}, which agree within one standard deviation, consistent with the hypothesis that they bind the same site. Across all f_{Co}, we found the predicted binding curves adequately predicted the experimental data (Fig. 3). At higher f_{Co} values, the experimental data reached saturation faster as a function of $[Ni^{II}]_{total}$ than at lower f_{Co}, which can be explained by the larger amount of total metal (nickel + cobalt) for a given $[Ni^{II}]_{total}$ value and is consistent with the behaviour predicted by the model.

The single-site model formulated in (Sect. 2.2) does not account for different F_{max} values observed for nickel *vs.* zinc. Modifying the single-site model to account for the different F_{max} values observed for nickel and zinc, however, still did not predict the Ni^{II}+Zn^{II} data adequately (Supplementary Fig. S2 and Supplementary Table S4). The drastically different F_{max} values inferred for zinc compared to nickel (Table 1) may be suggestive of different *Cc*NikZ-II binding mechanisms for nickel *vs.* zinc, such as binding unique binding sites on *Cc*NikZ-II. The hypothesis of a separate binding site for zinc is likewise consistent with zinc's preference for a tetrahedral geometry [7], whereas *Cc*NikZ-II's known nickel binding site exhibits octahedral geometry [32]. Thus, we then assessed the ability of the two-site model (2.3) to explain binding curves for *Cc*NikZ-II in solutions with nickel and zinc (Fig. 4). To obtain binding curves for *Cc*NikZ-II

in solutions with nickel and zinc, we titrated the protein with metal stock solutions containing a mixture of the two metals at a fixed total metal ratios of $f_{\text{Zn}} := [\text{Zn}^{\text{II}}]_{\text{total}}/[\text{Ni}^{\text{II}}]_{\text{total}} = 0.1$, 0.5, 1.0, 2.0, and 10.0. F_{obs} was measured for each f_{Zn} value over $[\text{Ni}^{\text{II}}]_{\text{total}}$ values between 0 μM and 250μM with $[P]_{\text{total}} = 0.4$ μM. We imposed the $K_{\text{D(Ni}^{\text{II}})}$, $K_{\text{D(Zn}^{\text{II}})}$, $F_{\text{max}}^{(1)}$, $F_{\text{max}}^{(2)}$ values determined in Sect. 3.1 (Table 1), leaving $F_{\text{max}}^{(1,2)}$ as the only free parameter in the two-site model for this system. Since $F_{\text{max}}^{(1,2)}$ is the only free parameter and it should be an intrinsic property of the protein (*i.e.* independent of f_{Zn}), we fit the two-site model to the data aggregated across all f_{Zn} values. Across all f_{Zn} values, we found the adequate agreement between the resulting curves and the experimental data. Like in Ni^{II}+Co^{II} systems, higher f_{Zn} values, the experimental data reached saturation faster than lower f_{Zn}, which can be explained by the larger amount of total metal (nickel + zinc) for a given $[\text{Ni}^{\text{II}}]_{\text{total}}$ value and is consistent with the behaviour predicted by the model. However, unlike the nickel + cobalt system, the experimental binding curves do not saturate to a constant value across all total metal ratios, a feature which is also captured by the fitted curves.

While we cannot rule out all possible alternative models from describing the data, we found that the single-site model (Sect. 2.2) adequately predicted the Ni^{II}+Co^{II} data using parameter values obtained in independent experiments without any additional curve-fitting (Fig. 3). This provides further evidence of the validity of the inferred parameters from the single-metal experiments (Sect. 3.1) and suggests that the single-site binding model may be representative of the mechanistic details of the binding dynamics of *Cc*NikZ-II in the Ni^{II}+Co^{II} system. Given the single-site model made adequate predictions for the Ni^{II}+Co^{II} system, we did not evaluate the two-site model against the Ni^{II}+Co^{II} data since the introduction of an additional fit parameter would trivially give rise to equal or better agreement with the data. Conversely, we found the single-site model did not adequately predict the Ni^{II}+Zn^{II} data even when the difference in F_{max} values for each metal was accounted for (Supplementary Fig. S2 and Supplementary Table S4). However, we found the two-site (Sect. 2.2) model adequately explained the data (Fig. 4. While comparison between the two-site model and the Ni^{II}+Zn^{II} data relied on fitting for $F_{\text{max}}^{(1,2)}$, the adequate agreement of the fitted curves across each f_{Zn} value suggests the two-site model may describe the binding dynamics of *Cc*NikZ-II in the Ni^{II}+Zn^{II} system. Given the adequate agreement of the proposed models and the data for both the Ni^{II}+Co^{II} and Ni^{II}+Zn^{II} systems, we proceeded with using the model to understand how changes in $K_{\text{D(Ni}^{\text{II}})}$ and $K_{\text{D(Co}^{\text{II}})}$ or $K_{\text{D(Zn}^{\text{II}})}$ could alter the fraction of competitor-bound *Cc*NikZ-II in each system (Sect. 3.3), which could be used to guide protein engineering efforts towards more selective binders for target metals (in this case nickel).

Table 2: Fitted Parameter and χ_r^2 for Ni^{II}+Zn^{II} Experiments

	$F_{\text{max}}^{(1,2)}$ (a.u.)	χ_r^2
Ni^{II} + Zn^{II} experiments (Fig. 4)	1048.2 ± 24.6	3.8

3.3 Model-based prediction of binding specificity over varying binding affinities

A goal of metalloprotein engineering is to improve a protein's specificity towards a particular target metal. This objective can be met either by 1) increasing the protein's binding affinity for the target metal (here, this corresponds to decreasing $K_{\text{D(Ni}^{\text{II}})}$), or 2) decreasing its binding affinity for non-target metals (here, this corresponds to increasing $K_{\text{D(Co}^{\text{II}})}$ or $K_{\text{D(Zn}^{\text{II}})}$). While the qualitative effects of altering these affinities may be intuitive (increased affinity for target metal or decreased affinity for competitor metals reduces binding specificity), the degree to which the equilibrium fraction of competitor-bound protein complexes (here, given by $[\text{Co}^{\text{II}}]_{\text{bound}}/[P]_{\text{total}}$ or $[\text{Zn}^{\text{II}}]_{\text{bound}}/[P]_{\text{total}}$, where $[\text{Co}^{\text{II}}]_{\text{bound}} = [\text{Co-}P]$ and $[\text{Zn}^{\text{II}}]_{\text{bound}} = [\text{Zn-}P] + [\text{Zn-}P\text{-Ni}]$) changes quantitatively with respect to changing K_{D} values is non-trivial.

We generated theoretical predictions for the competition fraction $[\text{Co}^{\text{II}}]_{\text{bound}}$ with $[P]_{\text{total}} = 0.4$ μM and $f_{\text{Co}} = 0.1,\ 1,$ and 10 using our validated specificity model (*c.f.* Sect. 2.2) for the Ni^{II}+Co^{II} system as a function of the fold change in 1) $K_{\text{D(Ni}^{\text{II}})}$ with $K_{\text{D(Co}^{\text{II}})}$ kept constant at the value determined in Sect. 3.1 (Table 1) (Fig. 5 A, C, E), and 2) $K_{\text{D(Co}^{\text{II}})}$ with $K_{\text{D(Ni}^{\text{II}})}$ kept constant at the value determined in Sect. 3.1 (Table 1) (Fig. 5 B, D, F) for several $[\text{Ni}^{\text{II}}]_{\text{total}}$ values. The range of the K_{D} values on these plots are restricted according to *Cc*NikZ-II's natural K_{D} values for cobalt and nickel and direction the values need to be altered to increase specificity.

For the Ni^{II}+Co^{II} system, where the validated model (Sect. 3.2) predicts nickel and cobalt compete for a shared binding site on *Cc*NikZ-II (Sect. 2.2), we first considered the hypothetical case where $K_{\text{D(Ni}^{\text{II}})}$ and $K_{\text{D(Co}^{\text{II}})}$ can be altered independently. In this case the model predicted that a given fold change in $K_{\text{D(Ni}^{\text{II}})}$ would give rise to comparable

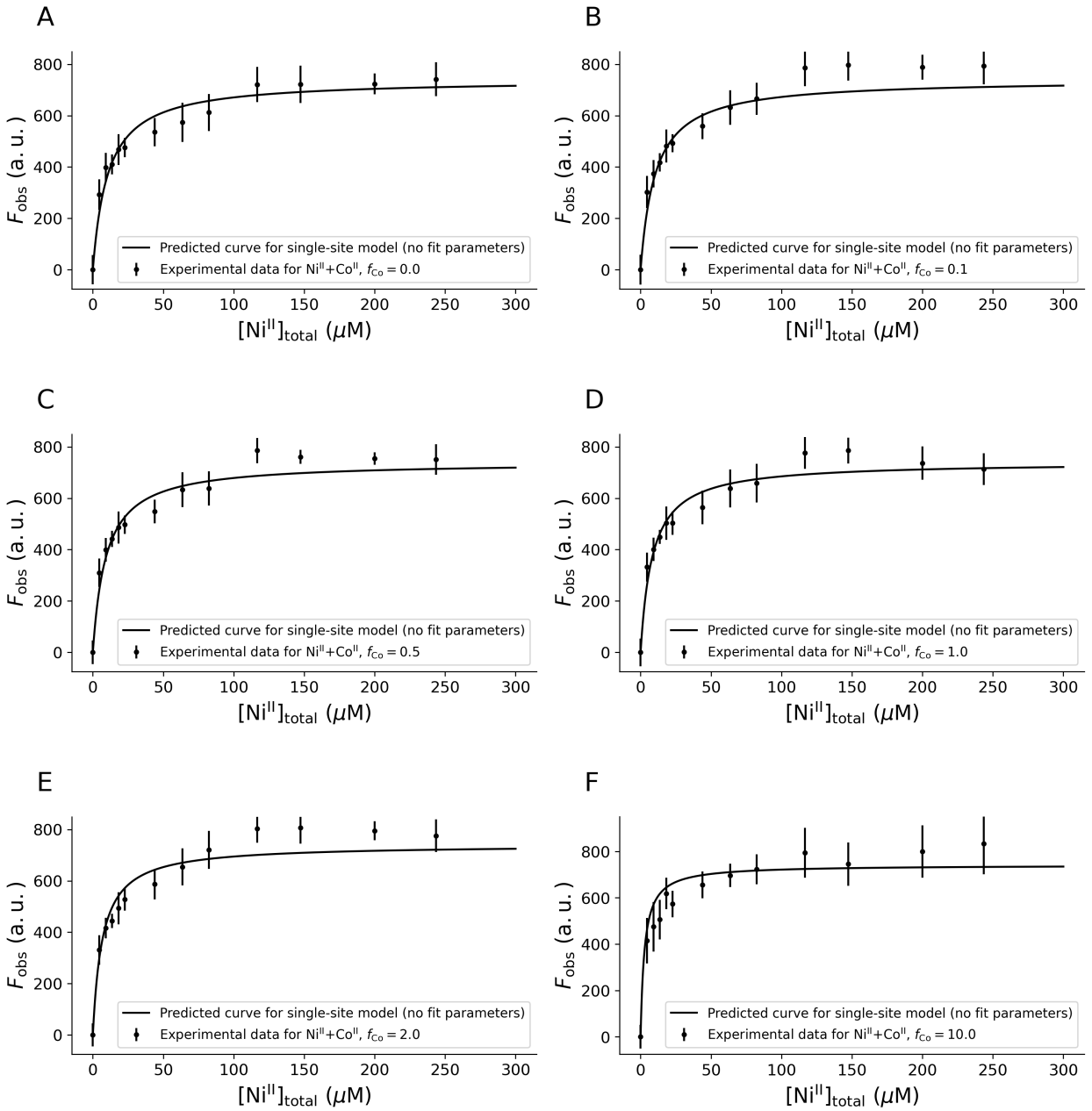

Figure 3: **Model validation by prediction of binding curves for varying f_{Co}.** *Cc*NikZ-II was titrated with cobalt-nickel mixtures of varying ratios (f_{Co} = 0.1 to 10) until saturation. The theoretically predicted (no fit) binding curves for the single-site model are plotted to evaluate the agreement of the model with the data. Experiments were performed in triplicate, n=3. The dots and error bars denote the mean and standard deviation, respectively, across the technical replicates for each titration step.

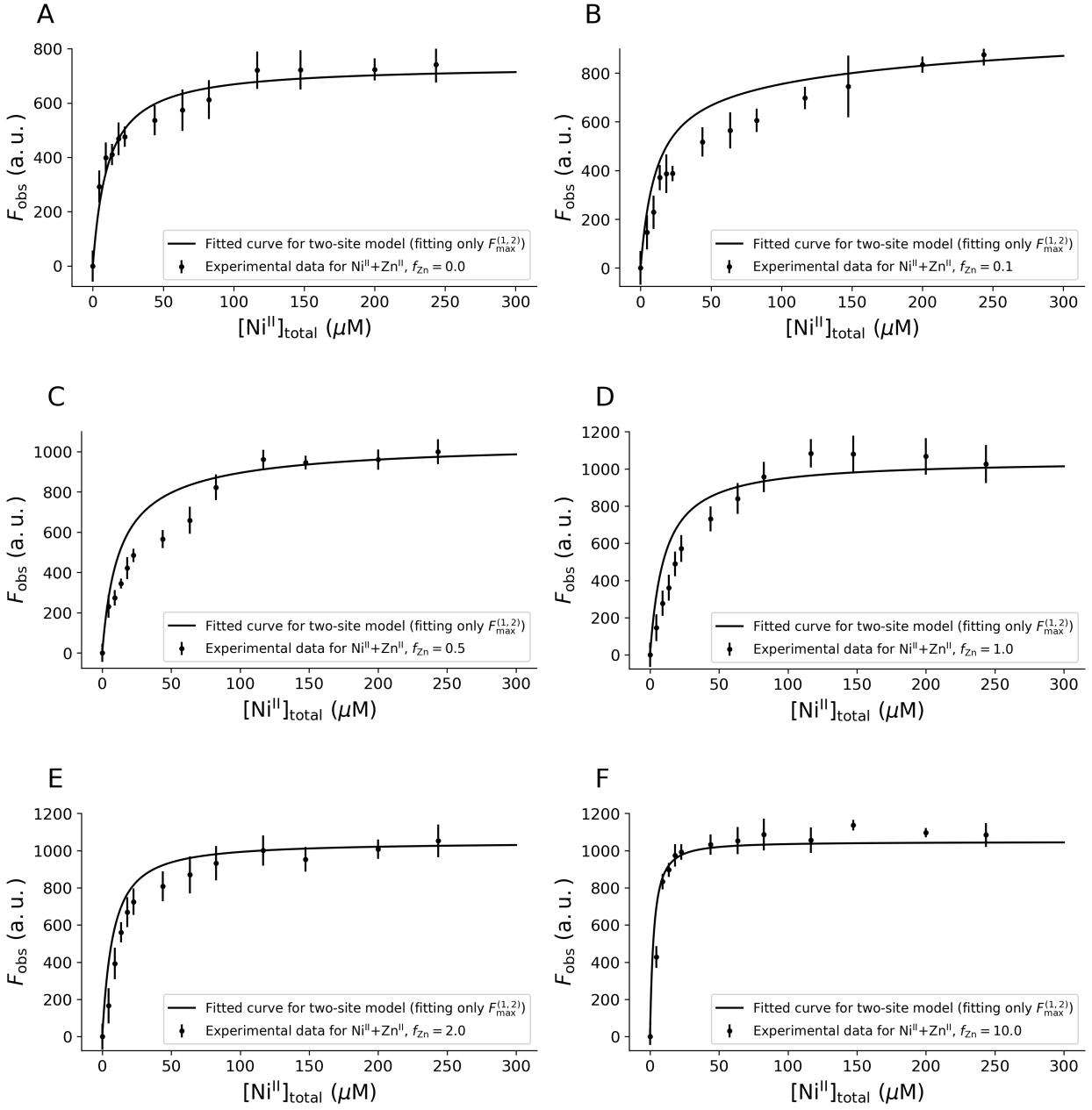

Figure 4: **Model validation by prediction of binding curves for varying f_{Zn}.** *Cc*NikZ-II is titrated with zinc-nickel mixtures of varying ratios (f_{Zn} = 0 to 10) until saturation. The fitted binding curves for the single-site model are plotted to evaluate the agreement of the model with the data. Note that the only free fit parameter is $F_{max}^{(1,2)}$, which was fitted to the data aggregated across all f_{Zn} values. Experiments were performed in triplicate, n=3. The dots and error bars denote the mean and standard deviation, respectively, across the technical replicates for each titration step.

changes in the specificity fraction for an equivalent fold change in $K_{\mathrm{D(Co^{II})}}$, with the exception of sufficiently small $[\mathrm{Ni^{II}}]_{\mathrm{total}}$ values where the specificity fraction becomes marginally more sensitive to fold changes in $K_{\mathrm{D(Co^{II})}}$ (Fig. 5).

In practice it may be difficult to change $K_{\mathrm{D(Ni^{II})}}$ and $K_{\mathrm{D(Co^{II})}}$ independently when nickel and cobalt share the same binding site, as predicted. Thus, we then considered how the specificity fraction changes when $K_{\mathrm{D(Ni^{II})}}$ and $K_{\mathrm{D(Co^{II})}}$ change together while holding their ratio constant. The ratio of dissociation constants for metals M_1 and M_2 defines the exchange constant K_{ex} for those metals and is commonly used to quantify the protein's relative binding specificity M_1 *vs.* M_2 [14]. Taking $M_1 = \mathrm{Ni^{II}}$ and $M_2 = \mathrm{Co^{II}}$, the exchange constant is mathematically given as

$$K_{\mathrm{ex}} = K_{\mathrm{D(Ni^{II})}}/K_{\mathrm{D(Co^{II})}} \; . \tag{16}$$

Intuitively, it is expected that a smaller K_{ex} corresponds to increased specificity for $\mathrm{Ni^{II}}$ relative to $\mathrm{Co^{II}}$. In the limit that $[\mathrm{Ni^{II}}]_{\mathrm{total}} \gg [P]_{\mathrm{total}}$ there is a simple quantitative relationship between the specificity fraction and K_{ex} for the single-site model (Sect. 2.2):

$$\lim_{\frac{[\mathrm{Ni^{II}}]_{\mathrm{total}}}{[P]_{\mathrm{total}}} \to \infty} \frac{[\mathrm{Co^{II}}]_{\mathrm{bound}}}{[P]_{\mathrm{total}}} = \frac{K_{\mathrm{ex}}}{K_{\mathrm{ex}} + f_{\mathrm{Co}}^{-1}} \; , \tag{17}$$

which confirms this intuition (see Supplementary Information Sect. S1.3 for derivation). The value of $\frac{[\mathrm{Ni^{II}}]_{\mathrm{total}}}{[P]_{\mathrm{total}}}$ predicted by the single-site model for intermediate $[\mathrm{Ni^{II}}]_{\mathrm{total}}$ values also confirms this intuition (Fig. 5). However, for intermediate $[\mathrm{Ni^{II}}]_{\mathrm{total}}$ values K_{ex} alone does not determine the specificity fraction for a fixed f_{Co} (Fig. 6). Moreover, this analysis predicts that the dissociation constant for the target metal (nickel) should be increased to achieve improved specificity over the competitor (cobalt) if the exchange constant remains constant for competing metals sharing the same binding site.

For the $\mathrm{Ni^{II}}$+$\mathrm{Zn^{II}}$ system, where the validated model (Sect. 3.2) predicts nickel and zinc bind unique binding sites on *Cc*NikZ-II (Sect. 2.3), the model predicts changing the target metal's dissociation constant ($K_{\mathrm{D(Ni^{II})}}$) has no effect on the fraction of $\mathrm{Zn^{II}}$-bound *Cc*NikZ-II complexes, while this quantity is decreased by increasing $K_{\mathrm{D(Zn^{II})}}$, as expected. In particular, since the binding of nickel and zinc are decoupled in such a model, both the fraction of nickel-bound and zinc-bound *Cc*NikZ-II is simply given by the bound-fraction expression Eq. (5) for the single-metal model (Sect. 3.1).

3.4 Limitations of the study

A protein's F_{max} can differ between different metals due to differences in binding characteristics (*e.g.*, differences in coordination geometry or binding sites). The F_{max} can also be affected by the protein's environmental conditions (*e.g.*, pH or temperature) and age. Earlier trials for the $\mathrm{Ni^{II}}$+$\mathrm{Co^{II}}$ experiments (not reported) resulted in binding curves that could not be adequately predicted by the specificity model Eq. (8), but was corrected by including a temperature equilibration step at 25°C prior to metal titrations. Additionally, *Cc*NikZ-II samples stored for long periods of time at 4 °C also experienced a reduction in the F_{max} (Supplementary Fig. S2), likely due to natural denaturation over time, similar to the activity of enzymes. This was corrected for by preparing fresh *Cc*NikZ-II solutions from freezer stocks. Failing to account for these conditions may result in different F_{max} values that may be incorrectly attributed to the nature of the binding event between a metal and protein.

There are also limitations related to model validation. While the binding curves predicted for the $\mathrm{Ni^{II}}$+$\mathrm{Co^{II}}$ experiments using the parameters inferred from the single-metal experiments appeared to predict the data adequately, the χ_r^2 value for each single-metal fit was less than one (Table 1). This suggests either over-fitting or overestimated variance. We suggest the latter is likely due to each fit involving only two free parameters and the calculated χ_r^2 being less than one for the theoretical predictions (no fit) for most of the $\mathrm{Ni^{II}}$+$\mathrm{Co^{II}}$ experiments (Supplementary Table S1). We found that accounting for the different F_{max} values observed for nickel binding *vs.* zinc binding with a two-site binding model (Sect. 2.3) could reasonably explain the data (Fig. 4). However, the χ_r^2 value for the two-site model fit to the $\mathrm{Ni^{II}}$+$\mathrm{Zn^{II}}$ data was greater than one for the aggregated data that $F_{\mathrm{max}}^{(1,2)}$ was estimated from (Table 2). This suggests either the fit did not fully capture the data or the data variance was underestimated. Likewise, the calculated χ_r^2 was greater than one when calculated for each $f_{\mathrm{Zn}} \neq 0$ (Supplementary Table S2). Given the previous arguments suggesting the data variance may be over-estimated, additional model features may be necessary to fully capture the data (*e.g.* cooperative binding resulting from allosteric interactions in the two-site model). Future work could explore these additional model complexities. Furthermore, while we showed reasonable agreement between our models and our data, it is impossible to rule out all possible alternative models due to the multiplicity of options. Future work could also explore additional validation approaches for the models, such as applying molecular dynamics simulations to verify stoichiometric and binding site multiplicity assumptions for particular multi-metal solutions.

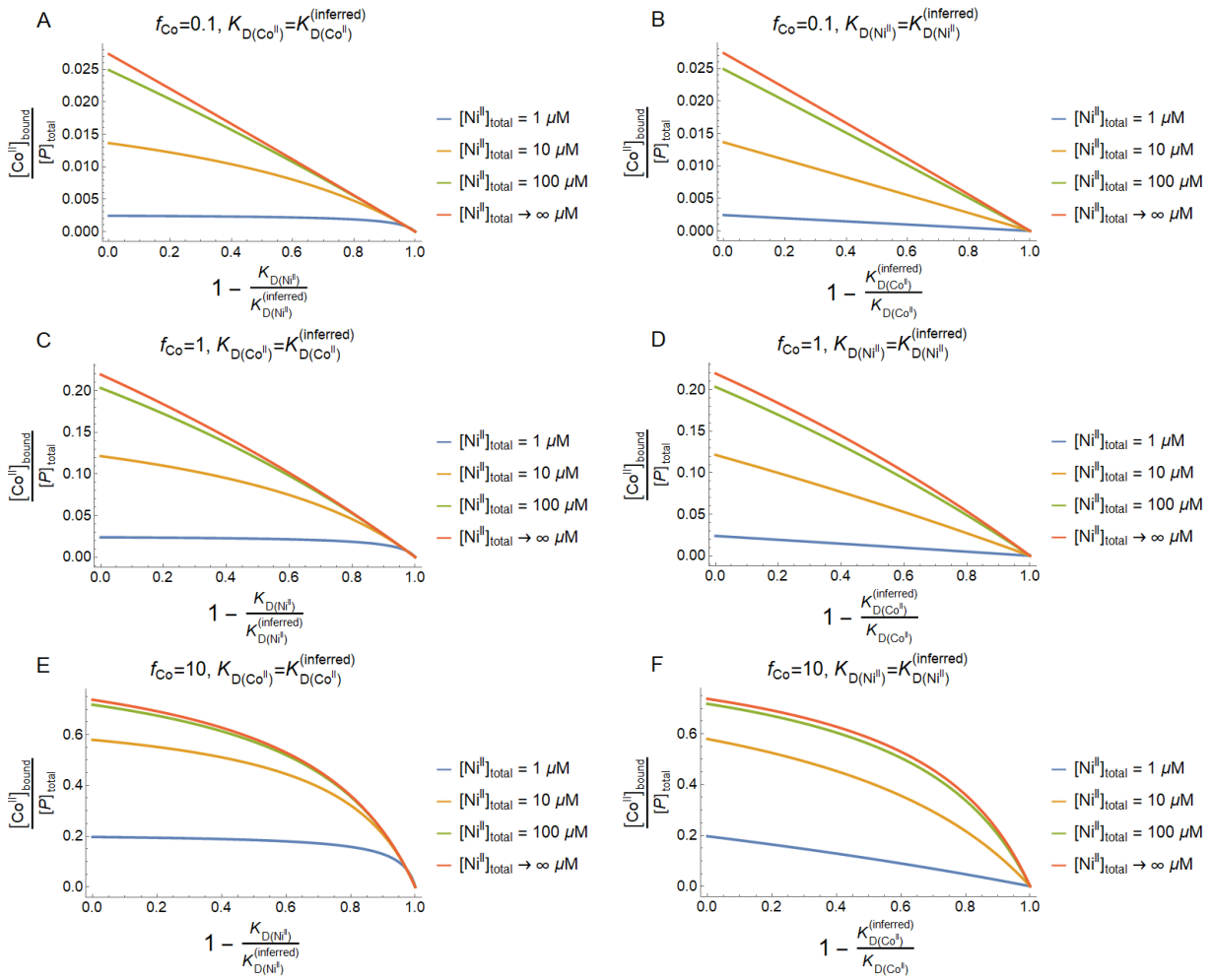

Figure 5: **Predicting specificity fraction in Ni^{II}+Co^{II} systems for individually varied metal binding affinities.** Keeping $K_{D(Co^{II})}$ constant at the value inferred via least squares optimization ($K^{(inferred)}_{D(Co^{II})}$) (Table 1), the specificity fraction is plotted as a function of $K_{D(Ni^{II})}$ for $[Ni^{II}]_{total} = 1,\ 10,\ 100$ μM across $f_{Co} = 0.1,\ 1,\ 10$ (A, C, E) for $[P]_{total} = 0.4$ μM. Similarly, keeping $K_{D(Ni^{II})}$ constant at the value inferred via least squares optimization ($K^{(inferred)}_{D(Ni^{II})}$) (Table 1), the specificity fraction is plotted as a function of $K_{D(Co^{II})}$ for $[Ni^{II}]_{total} = 1,\ 10,\ 100$ μM across $f_{Co} = 0.1,\ 1,\ 10$ (B, D, F) for $[P]_{total} = 0.4$ μM. The $[Ni^{II}]_{total} \gg [P]_{total}$ limit of the specificity fraction specified by Eq. (17) is also shown for each f_{Co} value.

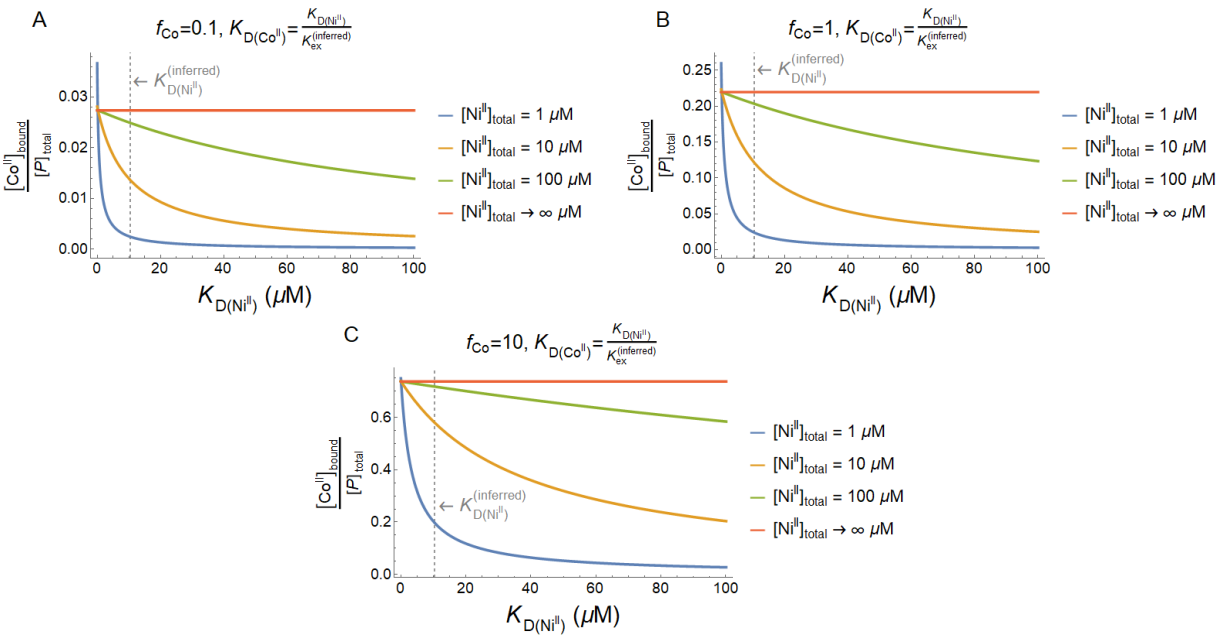

Figure 6: **Predicting specificity fraction in Ni^{II}+Co^{II} systems for varied metal binding affinities while fixing the exchange constant.** Fixing K_{ex} at at the value calculated from K_D values inferred via least squares optimization ($K_{ex}^{(inferred)}$) (Table 1), the specificity fraction is plotted as a function of $K_{D(Ni^{II})}$ for $[Ni^{II}]_{total} = 1,\ 10,\ 100$ µM across $f_{Co} = 0.1,\ 1,\ 10$ (A, B, C) for $[P]_{total} = 0.4$ µM. The $[Ni^{II}]_{total} \gg [P]_{total}$ limit of the specificity fraction specified by Eq. (17) is also shown for each f_{Co} value.

4 Conclusion

In this work we demonstrated a general high-throughput experimental approach relying on microplate-based assaying and intrinsic tryptophan fluorescence quenching to validate kinetic models for metalloproteins in solutions with multiple metals. Using our assay, we tested simple models describing the *in vitro* metal-binding dynamics of *Cc*NikZ-II in two-metal solutions. We found that different models were needed to adequately describe the measured binding curves in solutions consisting of Ni^{II}+Co^{II} *vs.* Ni^{II}+Zn^{II}. These different models make qualitatively different predictions for how changes in K_D for each metal species affects the protein's binding specificity for Ni^{II} and that the commonly used exchange constant does not uniquely determine binding specificity in general. This illustrates how mechanistic models could suggest design principles to guide the improvement of a metalloprotein's binding specificity and that these principles depend on the composition of solutions in prospective bio-remediation applications. With emerging research on *de novo* designed proteins [35, 36] that have anti-Irving-William series properties, our work here lays the groundwork for understanding how these synthetic proteins could be further engineered towards specific recovery of target metals from wastewater samples that contain more competing metals higher in the Irving-William series.

Acknowledgments

We thank Shay Tal for providing constructive comments on an earlier version of the manuscript.

Code availability

Code used for curve-fitting and calculating theoretical equilibrium concentrations is available on reasonable request from the corresponding author.

Contributors' statement

PD: Conceptualization, Investigation, Data curation, Methodology, Validation, Visualization, Writing - Original Draft, Review & Editing. BK: Conceptualization, Formal analysis, Methodology, Software, Validation, Visualization, Writing

- Original Draft, Review & Editing. AY: Supervision, Writing - Review & Editing. AH: Supervision, Writing - Review & Editing. RM: Supervision, Writing - Review & Editing.

References

[1] K. J. Waldron, J. C. Rutherford, D. Ford, and N. J. Robinson, "Metalloproteins and metal sensing," *Nature*, vol. 460, no. 7257, pp. 823–830, 2009.

[2] H. Irving and R. J. P. Williams, "The stability of transition-metal complexes," *J. Chem. Soc.*, no. 0, pp. 3192–3210, 1953. The Royal Society of Chemistry.

[3] J. A. Cotruvo, Jr and J. Stubbe, "Metallation and mismetallation of iron and manganese proteinsin vitro and in vivo: the class I ribonucleotide reductases as a case study," *Metallomics*, vol. 4, no. 10, pp. 1020–1036, 2012.

[4] D. Osman, M. A. Martini, A. W. Foster, J. Chen, A. J. P. Scott, R. J. Morton, J. W. Steed, E. Lurie-Luke, T. G. Huggins, A. D. Lawrence, E. Deery, M. J. Warren, P. T. Chivers, and N. J. Robinson, "Bacterial sensors define intracellular free energies for correct enzyme metalation," *Nature Chemical Biology*, vol. 15, no. 3, pp. 241–249, 2019.

[5] T. R. Young, M. A. Martini, A. W. Foster, A. Glasfeld, D. Osman, R. J. Morton, E. Deery, M. J. Warren, and N. J. Robinson, "Calculating metalation in cells reveals CobW acquires Co^{II} for vitamin B12 biosynthesis while related proteins prefer Zn^{II}," *Nature Communications*, vol. 12, no. 1, p. 1195, 2021.

[6] T. Dudev and C. Lim, "Competition among metal ions for protein binding sites: Determinants of metal ion selectivity in proteins," *Chemical Reviews*, vol. 114, no. 1, pp. 538–556, 2014.

[7] S. Barber-Zucker, B. Shaanan, and R. Zarivach, "Transition metal binding selectivity in proteins and its correlation with the phylogenomic classification of the cation diffusion facilitator protein family," *Scientific Reports*, 2017.

[8] J. A. Mattocks, J. A. Cotruvo, and G. J.-P. Deblonde, "Engineering lanmodulin's selectivity for actinides over lanthanides by controlling solvent coordination and second-sphere interactions," *Chemical Science*, vol. 13, no. 20, pp. 6054–6066, 2022. publisher: The Royal Society of Chemistry.

[9] T. R. Young and Z. Xiao, "Principles and practice of determining metal–protein affinities," *Biochemical Journal*, vol. 478, no. 5, pp. 1085–1116, 2021.

[10] K. B. Handing, E. Niedzialkowska, I. G. Shabalin, M. L. Kuhn, H. Zheng, and W. Minor, "Characterizing metal-binding sites in proteins with x-ray crystallography," *Nature Protocols*, 2018.

[11] K. A. Harnden, A. Roy, and P. Hosseinzadeh, "Overview of methods for purification and characterization of metalloproteins," *Current Protocols*, vol. 1, no. 8, p. e234, 2021.

[12] P. R. Callis, "Binding phenomena and fluorescence quenching. I: Descriptive quantum principles of fluorescence quenching using a supermolecule approach," *Journal of Molecular Structure*, vol. 1077, pp. 14–21, 2014.

[13] P. R. Callis, "Binding phenomena and fluorescence quenching. II: Photophysics of aromatic residues and dependence of fluorescence spectra on protein conformation," *Journal of Molecular Structure*, vol. 1077, pp. 22–29, 2014.

[14] Z. Xiao and A. G. Wedd, "The challenges of determining metal–protein affinities," *Natural Product Reports*, vol. 27, no. 5, p. 768, 2010.

[15] A. Treffry, Z. Zhao, M. A. Quail, J. R. Guest, and P. M. Harrison, "The use of zinc(II) to probe iron binding and oxidation by the ferritin (EcFtnA) of *Escherichia* coli," *JBIC Journal of Biological Inorganic Chemistry*, vol. 3, no. 6, pp. 682–688, 1998.

[16] B. A. Krizek, D. L. Merkle, and J. M. Berg, "Ligand variation and metal ion binding specificity in zinc finger peptides," *Inorganic Chemistry*, vol. 32, no. 6, pp. 937–940, 1993. publisher: American Chemical Society.

[17] W. Bal, J. Christodoulou, P. J. Sadler, and A. Tucker, "Multi-metal binding site of serum albumin," *Journal of Inorganic Biochemistry*, vol. 70, no. 1, pp. 33–39, 1998.

[18] W. Kou, H. S. Kolla, A. Ortiz-Acevedo, D. C. Haines, M. Junker, and G. R. Dieckmann, "Modulation of zinc- and cobalt-binding affinities through changes in the stability of the zinc ribbon protein l36," *JBIC Journal of Biological Inorganic Chemistry*, vol. 10, no. 2, pp. 167–180, 2005.

[19] A. Urvoas, M. Moutiez, C. Estienne, J. Couprie, E. Mintz, and L. Le Clainche, "Metal-binding stoichiometry and selectivity of the copper chaperone CopZ from *Enterococcus hirae*," *European Journal of Biochemistry*, vol. 271, no. 5, pp. 993–1003, 2004.

[20] L. Zhang, M. Koay, M. J. Maher, Z. Xiao, and A. G. Wedd, "Intermolecular transfer of copper ions from the CopC protein of pseudomonas syringae. crystal structures of fully loaded Cu(I)Cu(II) forms," *Journal of the American Chemical Society*, vol. 128, no. 17, pp. 5834–5850, 2006. publisher: American Chemical Society.

[21] J. M. Berg and D. L. Merkle, "On the metal ion specificity of zinc finger proteins," *Journal of the American Chemical Society*, vol. 111, no. 10, pp. 3759–3761, 1989. publisher: American Chemical Society.

[22] Z. Dong, J. A. Mattocks, G. J.-P. Deblonde, D. Hu, Y. Jiao, J. A. Cotruvo, and D. M. Park, "Bridging hydrometallurgy and biochemistry: A protein-based process for recovery and separation of rare earth elements," *ACS Central Science*, vol. 7, no. 11, pp. 1798–1808, 2021. publisher: American Chemical Society.

[23] K. P. Cannell and J. B. Vincent, "Metal ion concentration, time, and pH dependence of metal ion binding to a transferrin metalloprotein affinity chromatography (MAMC) matrix," *Journal of Chemical Technology & Biotechnology*, vol. 64, no. 1, pp. 96–100, 1995.

[24] K. Spires and J. B. Vincent, "Transferrin metalloprotein affinity metal chromatography," *Journal of Chemical Technology & Biotechnology*, vol. 62, no. 4, pp. 373–379, 1995.

[25] M. van de Weert and L. Stella, "Fluorescence quenching and ligand binding: A critical discussion of a popular methodology," *Journal of Molecular Structure*, vol. 998, no. 1, pp. 144–150, 2011.

[26] D. Beckett, "Measurement and Analysis of Equilibrium Binding Titrations: A Beginner's Guide," *Methods in Enzymology*, vol. 488, pp. 1–16, jan 2011.

[27] C. Micaloni, G. K. Kong, A. P. Mazzetti, M. Nuccetelli, G. Antonini, L. Stella, W. J. McKinstry, G. Polekhina, J. Rossjohn, G. Federici, G. Ricci, M. W. Parker, M. Lo Bello, and R. Huber, "Engineering a New C-terminal Tail in the H-site of Human Glutathione Transferase P1-1: Structural and Functional Consequences," *Journal of Molecular Biology*, vol. 325, pp. 111–122, jan 2003.

[28] D. D. Perrin and I. G. Sayce, "Computer calculation of equilibrium concentrations in mixtures of metal ions and complexing species," *Talanta*, vol. 14, no. 7, pp. 833–842, 1967.

[29] J. R. Pradines, J. Hasty, and K. Pakdaman, "Complex ligand-protein systems: a globally convergent iterative method for the n×m case," *Journal of Mathematical Biology 2001 43:4*, vol. 43, no. 4, pp. 313–324, 2001.

[30] John R.Taylor, *An Introduction to Error Analysis*. University Science Books, 2 ed., 1997.

[31] J. J. Almagro Armenteros, K. D. Tsirigos, C. K. Sønderby, T. N. Petersen, O. Winther, S. Brunak, G. von Heijne, and H. Nielsen, "SignalP 5.0 improves signal peptide predictions using deep neural networks," *Nature Biotechnology*, vol. 37, no. 4, pp. 420–423, 2019. Number: 4 publisher: Nature Publishing Group.

[32] P. Diep, R. Mahadevan, and A. F. Yakunin, "A microplate screen to estimate metal-binding affinities of metalloproteins," *Analytical Biochemistry*, vol. 609, p. 113836, 2020.

[33] R. M. Howlett, B. M. Hughes, A. Hitchcock, and D. J. Kelly, "Hydrogenase activity in the foodborne pathogen *Campylobacter jejuni* depends upon a novel ABC-type nickel transporter (NikZYXWV) and is SlyD-independent," *Microbiology*, vol. 158, no. 6, pp. 1645–1655, 2012. publisher: Microbiology Society,.

[34] H. Lebrette, C. Brochier-armanet, B. Zambelli, H. de Reuse, E. Borezée-Durant, S. Ciurli, and C. Cavazza, "Promiscuous nickel import in human pathogens: Structure, thermodynamics, and evolution of extracytoplasmic nickel-binding proteins," *Structure*, vol. 22, no. 10, pp. 1421–1432, 2014.

[35] T. S. Choi and F. A. Tezcan, "Design of a flexible, Zn-selective protein scaffold that displays anti-Irving–Williams behavior," *Journal of the American Chemical Society*, vol. 144, no. 39, pp. 18090–18100, 2022.

[36] T. S. Choi and F. A. Tezcan, "Overcoming universal restrictions on metal selectivity by protein design," *Nature*, vol. 603, no. 7901, pp. 522–527, 2022.